American Mineralogist, Volume 75, pages 1311–1326, 1990

The solubility of carbon dioxide in rhyolitic melts: A quantitative FTIR study

ROBERT A. FOGEL,* MALCOLM J. RUTHERFORD
Department of Geological Sciences, Brown University, Providence, Rhode Island 02912, U.S.A.

ABSTRACT

The solubility of CO_2 in rhyolite liquid has been determined using quantitative Fourier-transform infrared spectroscopy (FTIR). CO_2 saturation experiments were conducted along isotherms at 950 °C, 1050 °C, and 1150 °C at pressures between 500 and 6600 bars. The band at 2350 cm^{-1}, which represents the antisymmetric stretch of dissolved CO_2 molecules, was used for quantitative determinations of CO_2 concentration.

The isotherm at 1050 °C was investigated in greatest detail. Along this isotherm CO_2 solubility is ideal (in the Henrian sense) up to ≈2300 bars. Above this pressure deviations from ideality are prominent, with concentrations less than predicted by extrapolation of the linear form of Henry's Law. The effect of increasing temperature is to decrease the solubility of molecular CO_2. The water contents of these glasses were also monitored using the 3570 cm^{-1} OH^- fundamental vibration. Maximum H_2O contents were 0.32 wt%.

The solubility of CO_2 in rhyolite has been modeled with a modified Henry's Law equation. The data were regressed to determine the partial molar volume ($\bar{v}$ = 33.04 ± 0.78 cm^3/mol) and the heat of solution (Δh = −20.32 ± 3.18 kJ/mol) of dissolved CO_2 (reference T = 1323 K and P = 0 bars).

CO_2 diffusion profiles were present in several samples. The diffusion coefficient of CO_2 in rhyolite at 1050 °C was estimated in three samples to be 2.4 (±0.5) × 10^{-8} cm^2/s, in close agreement with previous work.

A comparison of rhyolite and albite melts at low P and high T shows that the two compositions dissolve nearly identical amounts of molecular CO_2. This implies a CO_2 (molecular, hereafter Mol.) solubility mechanism that is comparable in both compositions. Divergence of CO_2(Mol.) solubility in albite and rhyolite at high P and low T is consistent with accentuated differences in melt structure at these conditions and differences in the siting of CO_2(Mol.) at high CO_2 concentrations.

Infrared bands attributable to dissolved carbonate complexes were not detected. This is consistent with the general decrease in the ratio of CO_3^{2-} to CO_2(Mol.) in the sequence basalt, andesite, rhyodacite, rhyolite observed in this study. Basalt dissolves CO_2 in the form of carbonate complexes, whereas rhyolite dissolves CO_2 in the molecular form. Somewhat more CO_2 dissolves in rhyolite than in basalt under similar conditions. The common contention that CO_2 is more soluble in mafic magmas than in more evolved compositions is incorrect.

INTRODUCTION

Magma genesis and evolution are often associated with a fluid phase in which CO_2 is an important component. This is particularly true of basaltic magmas, where CO_2 is generally the main component of the fluid phase (Dixon et al., 1988; Gerlach, 1986; Roedder, 1965). H_2O is an important volatile component in more silicic magmas, but CO_2 may be present in significant amounts and could play a critical role in the genesis, evolution, and eruption of high-silica magmas. The presence of CO_2 in silicic magmas has been confirmed by the analysis of melt inclusions trapped by phenocryst phases (Anderson et al., 1989; Sommer, 1977) and the analysis of obsidian fragments (Newman et al., 1988). Degassing, which accompanied the recent Mount Saint Helens eruptions, also indicates a significant fraction of CO_2 (1–10 mol%) in the magmatic fluid (Gerlach and Casadevall, 1986a, 1986b). Phase-equilibrium studies of the dacite pumice erupted from Mount Saint Helens on May 18, 1980 (Rutherford et al., 1985) and the Fish Canyon quartz latite (Johnson and Rutherford, 1989) are consistent with the magmas having been in equilibrium with an H_2O-CO_2 fluid. There is, therefore, ample evidence that CO_2 dissolves in silicic as well as basaltic magmas.

It is generally understood that CO_2 plays an important role in magmatic processes. Despite this recognition, current understanding of the physical and chemical effects

* Present address: American Museum of Natural History, W 79th St. at Central Park West, New York, New York 10024, U.S.A.

0003–004X/90/1112–1311$02.00

of CO_2 upon magma is still in its infancy. This appears to be an extension of the poor state of knowledge of the gaseous properties of CO_2, where the nonideality of CO_2 at high pressures and temperatures is still poorly known and the behavior of CO_2 in the presence of other magmatic fluid species is even less well understood.

With regard to magmatic evolution, the most important thermodynamic property of CO_2 is its solubility in silicate liquids. A detailed understanding of processes such as phase equilibrium, magma vesiculation, bubble growth, magma explosivity, and planetary atmospheric evolution all require reasonable estimates of CO_2 solubility. An understanding of CO_2 speciation within the silicate molecular structure is also of importance, as it leads to physically correct solution models and more accurate solubility predictions.

Although the significance of CO_2 solubility measurements has long been recognized, advances in this area were hindered by the lack of a reliable technique for measuring CO_2 concentrations. Most studies were consequently carried out at very high pressures (>10 kbar), where CO_2 solubility is appreciable, and the problems of CO_2 detection and analysis were less critical. Recently, Fine and Stolper (1985) made use of quantitative infrared spectroscopy (QIS) for determining CO_2 concentrations in liquid compositions of geological importance. QIS is a rapid, nondestructive technique that is capable of high spatial and compositional resolution. It has been used to study the solubility behavior of CO_2 in albite melt at 1450 °C–1625 °C and pressures of 15–30 kbar (Stolper et al., 1987), and the Henry's Law behavior of CO_2 in basaltic melt at 1200 °C and at pressures below 1500 bars (Stolper and Holloway, 1988).

The purpose of this study is to determine the solubility of CO_2 in rhyolite melt under a wide range of P and T. Our analytical method makes use of quantitative FTIR spectroscopy for determining both CO_2 solubility and speciation (molecular CO_2 vs. carbonate). Experiments were conducted at pressures between 500 and 6600 bars and at temperatures between 950 °C and 1150 °C. These experiments cover a pressure range that is governed by Henry's Law as well as higher pressure conditions where significant deviations from Henry's Law occur. The range in temperature allows extrapolation of the results to lower T as well as direct application to high-temperature rhyolitic volcanism. The temperature-pressure range investigated also allows a comparison of our work with that of Stolper and Holloway (1988) to address the common perception that CO_2 solubility is much greater in liquids of low silica activity (i.e., basalt), than liquids of high silica activity (i.e., rhyolite; e.g., Eggler and Rosenhauer, 1978; Carmichael et al., 1974).

Experimental techniques

Experimental procedure

Rhyolitic obsidian VNM50-15 from the Brown University collection was used in all experiments. VNM50-15 is an obsidian fragment from an unknown locality in the area of the Valles Caldera, New Mexico. It was chosen because its physical and chemical properties were ideal for this study. It is vitreous and free from vapor bubbles and silicate crystals (although occasional Fe-Ti oxide crystals on the order of a few micrometers across are present). Its composition (Table 1) is similar to highly evolved rhyolites such as the Upper Bandelier Tuff (Fogel, 1989) and the Bishop Tuff (Anderson et al., 1989). Normalized to the granite ternary (quartz-albite-orthoclase), VNM50-15 falls close to the minimum melting point at 3000 bar for H_2O-saturated granite (Tuttle and Bowen, 1958). The H_2O content of VNM50-15 as determined by IR analyses is 1366 ± 67 ppm by weight (ppmw) based on six analyses on a sample ≈17 mm².

Table 1. Electron microprobe analyses and CIPW norm of VNM50-15 starting material

Oxide	Wt%	σ	CIPW	Norm
SiO_2	76.45	(0.24)	q	33.12
TiO_2	0.08	(0.05)	or	28.22
Al_2O_3	12.56	(0.13)	ab	35.66
Fe_2O_3	N.D.	N.D.	an	1.24
FeO	1.02	(0.07)	ne	0.00
MnO	0.08	(0.07)	lu	0.00
MgO	0.06	(0.02)	di	0.00
CaO	0.25	(0.06)	ol	0.00
Na_2O	4.21	(0.11)	mt	0.00
K_2O	4.78	(0.21)	il	0.15
Total	99.48			

Note: Electron microprobe analysis of starting material VNM50-15 along with its CIPW Norm. All Fe is calculated as FeO. Parentheses indicate one standard deviation (1σ) on six microprobe analyses. N.D. = not determined.

Rectangular chips of VNM50-15 glass were cut with a diamond saw, ground to a weight of between 50 and 150 mg, cleaned with water, rinsed in ethanol, and dried. Samples were weighed and placed in $Ag_{70}Pd_{30}$ tubes welded shut at the bottom. One chip was used per tube, the approximate dimensions of which were 2.5 × 2.5 × 5 mm. Silver oxalate ($Ag_2C_2O_4$) was added to the tube in an amount far in excess of that required to saturate the sample in CO_2. The tube was welded shut and tested for leaks by weighing the tube, heating to 112 °C for a few minutes, and then rapidly quenching in H_2O. Leakage of the tube was determined by reweighing and checking for a H_2O weight gain.

Experiments were conducted in either TZM pressure vessels or an internally heated pressure vessel (IHPV). The TZM pressure vessels were used to investigate the low pressure region below 3000 bars and temperatures below 1100 °C. The internally heated pressure vessel was used for pressures greater than 3000 bars or temperatures in excess of 1100 °C. The pressurizing medium for both vessels was Ar. For the TZM experiments, pressure was measured on a bourdon tube Heise gauge (0–7000 bar) periodically calibrated at the factory. In the IHPV, experiments between 3000 and 6000 bars were measured on a THI transducer (0–6900 bar) calibrated at the factory. Experimental pressures in excess of 6000 bars were measured using a Harwood manganin cell (0–13800 bar)

and Foxboro gauge calibrated at the factory. Both IHPV pressure measuring devices were periodically checked against the Heise gauge for internal consistency. Reported pressures are accurate to better than 0.5% of full scale values.

Temperature was controlled by Eurotherm temperature controllers accurate to within ±3 °C. In the IHPV experiments, the sample sat in a cylindrical Pt container, the walls of which are 1 mm thick. Pt-$Pt_{90}Rh_{10}$ measuring and controlling thermocouples were inserted into a hole in the bottom of this container. This platinum-block assembly was used to minimize temperature gradients across the sample. Temperatures are considered to be within ±5 °C of that recorded. The TZM assembly consisted of a TZM alloy pressure vessel with an external inconel sheath. The charge sat at the bottom of the vessel and graphite rods took up most of the excess volume so as to minimize convection. A few bars of Ar pressure were constantly applied between the pressure vessel and the sheath to prevent oxidation of the TZM. As a consequence of this type of assembly, temperatures within the pressure vessel could not be measured during the experiments; temperatures within the vessel were calibrated at 1 atm of Ar pressure against the temperature in the sheath wall. The reproducibility of this calibration is ±5 °C. Temperatures in the TZM vessels are thought to be accurate to better than ±10 °C.

IHPV experiments were quenched by turning the power off and rotating the vessel 90° to disturb its thermal stability. Quench rates were on the order of 100 °C/s for the first 2–3 s of the quench. The TZM experiments were quenched by removing the vessel from the furnace and quenching in H_2O. TZM quench rates were on the order of 2–3 °C/s and produced glasses indistinguishable from those produced using the IHPV. After the experiment, the samples were weighed to check for weight loss. Upon cutting of the noble metal container, an audible hiss verified the presence of a CO_2 vapor phase and the integrity of the capsule. Experimental glasses were also examined under a binocular microscope for vapor bubbles, the presence of which lends support for the existence of a vapor phase during the run.

Vapor bubbles were present in almost all samples. Generally, these were a few micrometers in diameter, but bubbles on the order of hundreds of micrometers were sometimes present. Vesiculation occurred predominantly along the margins of the sample, and an examination of glass exteriors showed vapor bubble indentations. Vapor bubbles within the sample were most often found along planes, suggesting that bubble formation occurred along preexisting cracks in the glass sample. These observations suggest that the presence of vapor bubbles is mainly due to the physical incorporation of CO_2 vapor rather than vesiculation of the liquid upon the quench.

FTIR sample preparation and analytical technique

After preliminary examination, experimental glasses were cut into wafers and ground in a slurry of alumina and H_2O. Samples were generally ground to thicknesses of 100–300 μm and were polished on two parallel sides with alumina either 0.3 or 0.05 μm in diameter. FTIR sections were then examined under a microscope and a detailed sketch of the section made. Section thicknesses were mapped using a Mitutoyo digital dial indicator with a precision of roughly ±3 μm. This mapping was necessary because of the difficulty in making sections of uniform thickness. The fine spatial resolution of the micro-FTIR puts added emphasis on accurately determining sample thickness. An average thickness may lead to erroneous concentration determinations when spatial resolution is on the order of tens of micrometers.

FTIR spectra were performed on the Brown University IBM Instruments Model IR-98 (IFS-113v) FTIR spectrometer. All samples were analyzed with the micro-FTIR attachment. The microscope is equipped with an objective lens of 15× magnification. A set of apertures ranging in size from 1200–300 μm provided spatial resolution from 80–20 μm, respectively. Samples were positioned over apertures on a sample-holder slide. This assembly was placed on the microscope stage, and an area free from vesicles was chosen for analyses. In a few cases where micrometer-sized bubbles could not be avoided, spectra were taken of several areas relatively free from bubbles, and the CO_2 concentration was shown to be independent of bubble density. Spectra were taken using a globar source, a KBr beamsplitter, a HgCdTe detector, resolution of 4 cm^{-1}, a mirror velocity of 0.396 cm/s and either 128, 256, or 512 scans.

Quantitative IR spectroscopy

Theory

The relationship between concentration and IR band intensity is given by the Beer-Lambert law:

$$C = 10^6 \frac{MW \cdot Abs}{\rho \cdot \epsilon \cdot d} \quad (1)$$

where C is concentration in ppm by weight, MW is the molecular weight of the IR active component in g/mol (CO_2 = 44.01, H_2O = 18.02), Abs is the band intensity in dimensionless absorbance units, ρ is sample density in g/L, ϵ is the molar absorptivity or extinction coefficient of the IR band in L/(mol·cm), and d is the thickness of sample under the IR beam in cm.

Abs is measured from peak to baseline where the baseline is interpolated from the surrounding spectral range. Baseline interpolation is accomplished by drawing a line tangential to the baseline on both the high- and low-energy side of the band. In cases where silicate network vibrations overlap the band of interest or interfere with the smooth interpolation of baseline, spectral subtraction of a reference sample devoid of the absorbing species is used; the spectra of the reference being first normalized to the thickness of the unknown. Since the bands of interest in this study have smooth, noncomplicated backgrounds, spectral subtraction was not employed.

The density of VNM50-15 was measured using a 25 mL pycnometer. H_2O was used as the liquid-density medium, being first boiled and set to cool to 25 °C to eliminate dissolved O. A density of 997.05 g/L (Weast and Astle, 1981) was taken as the density of deionized H_2O at 25 °C to which the glass densities were referenced. The density of seven chips of VNM50-15 cumulatively weighing 0.89083 g was determined to be 2348 ± 10 g/L. All CO_2 solubility measurements were determined with this value. Incorporation of CO_2 into the experimental glasses was assumed to have a negligible effect on densities.

Since concentration is inversely proportional to sample thickness, analyses of an experimental sample at several thicknesses should retrieve the same total concentration. A Beer's Law test was conducted measuring CO_2 concentration (from the band at 2350 cm^{-1}) as a function of thickness and found to retrieve the same value consistently. The measured relative standard deviation on the concentration was 4%.

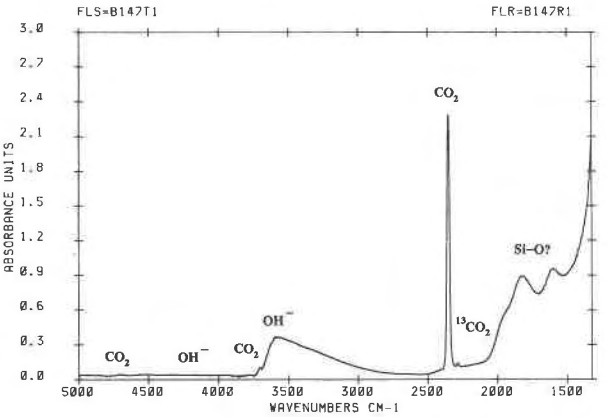

Fig. 1. Typical FTIR spectrum of a CO_2-saturated experimental glass. Band assignments are indicated above the respective bands. The experimental glass (BF147) contains 2860 ppmw CO_2 and 1921 ppmw H_2O.

Band assignments

An example of a typical FTIR spectrum of a CO_2-bearing rhyolite is shown in Figure 1. The spectral range of interest is the area between 5000 cm^{-1} and 1000 cm^{-1}. Several bands are present in this spectral region, each of which will be discussed individually.

The bands at 1375 and 1610 cm^{-1}. The doublet bands centered on 1375 and 1610 cm^{-1} are caused by the presence of dissolved carbonate (CO_3^{2-}). CO_2 in the form of carbonate appears to be the dominant form of CO_2 solution in basalt, diopside, and akermanite melts (Fine and Stolper, 1986; Rai et al., 1983; Sharma et al. 1979). At high pressures, it has also been shown to be present in sodium aluminosilicate melts (Stolper et al., 1987; Fine and Stolper, 1985). Unpublished work from this laboratory shows it to be an important species in andesite (56 wt% SiO_2) and rhyodacite (66 wt% SiO_2) melts produced at pressures below 3 kbar. None of the rhyolite experiments conducted for this study shows the presence of carbonate bands. Spectral subtraction of CO_2-free standard rhyolite material shows a flat pattern in this area, suggesting that if CO_2 dissolves as carbonate under the physical conditions investigated, it is present in amounts below detectability: ≈50–100 ppmw.

The bands at 1600 and 1820 cm^{-1}. Newman et al. (1986) attributed these bands to aluminosilicate network vibrations. Their work involving rhyolitic compositions similar to that used in this study found these bands did not correlate with H_2O content. This study shows no correlation of the intensity of these bands with CO_2 content. FTIR spectra of the compositional sequence basalt (49 wt% SiO_2), andesite (56 wt% SiO_2), rhyodacite (66 wt% SiO_2), and rhyolite (76 wt% SiO_2) show a clear growth of these bands. They are barely existent in basalt but grow in intensity and definition with increasing melt polymerization (SiO_2 content). Although most silicate network vibrations are present at energy levels below 1200 cm^{-1}, the combination of factors listed above tends to support the suggestion of Newman et al. (1986). We suggest, however, that because of the high energy levels of these bands, they may be combination or overtone bands of the aluminosilicate network.

The band at 2287 cm^{-1}. This band has been assigned to the ν_3 antisymmetric stretch of $^{13}CO_2$ molecules (Stolper et al., 1987; Fine and Stolper, 1985). It appears as a small band just off the shoulder of the high intensity band centered at 2350 cm^{-1}. Stolper et al. (1987) determined the extinction coefficient of this band (ϵ_{2287}) for molecular CO_2 in albite glass. Their value for ϵ_{2287} of 11.7 L/(mol·cm) was determined for the total CO_2(Mol.) in albite melt instead of the molecular $^{13}CO_2$ it represents. At low CO_2 concentrations this band is not very intense, but it is generally useful for the determination of high CO_2 concentrations.

The band at 2350 cm^{-1}. This band represents the ν_3 antisymmetric stretch of dissolved $^{12}CO_2$ molecules (Fine and Stolper, 1985). It is a sharp narrow band that is often the dominant spectral feature for glasses with moderate to high CO_2 concentrations. Its extinction coefficient in sodium aluminosilicate melts has been determined by Fine and Stolper (1985). They investigated the speciation of CO_2 along the join $NaAlO_2$-SiO_2 studying the $NaAlSi_2O_6$ (jadeite), $NaAlSi_3O_8$ (albite), and $NaAlSi_4O_{10}$ glass compositions. A single value for ϵ_{2350} of 945 ± 45 L/mol·cm) was determined for all three compositions.

The band at 2350 cm^{-1} is used in this study as the principal band for the determination of CO_2 solubility in rhyolite glasses. Since the only calibration for ϵ_{2350} in silicate compositions is for the $NaAlO_2$-SiO_2 join, there is some concern that the value of 945 L/(mol·cm) may not be appropriate to rhyolitic compositions. There is, however, reason to believe that the value of ϵ_{2350} established for the $NaAlO_2$-SiO_2 join is either directly applicable or quite close to ϵ_{2350} in rhyolite. Fine and Stolper (1985) showed that within the portion of the sodium-aluminosilicate join they investigated, ϵ_{2350} was independent of SiO_2

concentration. In addition, the composition $NaAlSi_4O_{10}$ in their study is roughly that of the albite-silica eutectic at 1 atm. The addition of orthoclase to the albite-silica system produces the granite ternary into which sample VNM50-15 projects with less than a 3% residual (Table 1). The combination of these factors suggests that the only influence, if any, on changing ϵ_{2350} for rhyolitic compositions from that determined for the sodium-aluminosilicates is the substitution of K_2O for Na_2O in the silicate structure. The addition of minute amounts of FeO, MgO, MnO, TiO_2, and CaO that total to no more than 3% is unlikely to have an effect on ϵ_{2350}.

The broadly similar behavior of K_2O and Na_2O in silicate glasses and crystals as well as molecular similarities suggests that ϵ_{2350} is little affected by the K_2O for Na_2O substitution. It is more intuitively satisfying, however, to note that the species under discussion is dissolved in the silicate melt in the molecular form—i.e., CO_2 appears to be trapped in holes in the melt and is not bonded to the aluminosilicate network. Although holes have potential fields, an alkali substitution is less likely to affect dissolved molecular species that would respond to changes in the size and shape of the holes they occupy than to affect species bonded to the network, which would respond to changes in composition and network structure. The extinction coefficients for the molecular and OH^- forms of H_2O in albite (Silver and Stolper, 1989) and rhyolite (Newman et al., 1986) glasses support this idea. For rhyolite and albite glass, the extinction coefficients for OH^- (4500 cm^{-1}) are 1.73 and 1.13 L/(mol·cm), whereas the extinction coefficients for the bands representing molecular H_2O are 1630 cm^{-1} = 55 and 49 L/(mol·cm) and 5200 cm^{-1} = 1.61 and 1.67 L/(mol·cm), respectively.

Ultimately, the value of the extinction coefficient used in the Beer-Lambert Law affects only the magnitude of CO_2 solubility. The ratio of two glasses of constant density with concentrations C_1 and C_2 yields

$$\frac{C_1}{C_2} = \frac{Abs_1/d_1}{Abs_2/d_2}, \quad (2)$$

demonstrating that CO_2 concentrations determined relative to each other are not dependent upon ϵ and can be used with confidence. If indeed ϵ_{2350} is shown to be significantly different in rhyolite than in albite glass, absolute CO_2 concentrations can be redetermined with the Beer-Lambert law and the updated value of ϵ_{2350}.

The band at 3570 cm^{-1}. The fundamental OH^- stretching vibration produces this broad band (Stolper 1982a). H_2O in the form of both H_2O(Mol.) and OH^- contributes to the intensity of this band. It is highly asymmetric with the maximum peak intensity occurring around 3570 cm^{-1}. This band is used in this study as the fundamental band for the determination of H_2O contents of the experimental glasses. Since total H_2O contents of experimental samples in this study were less than 0.32 wt% and bands attributable solely to molecular H_2O (5200 cm^{-1} and 1620 cm^{-1}) were not detected, the H_2O contents represented by the band at 3570 cm^{-1} represent only OH^- groups. The extinction coefficient in rhyolitic glasses for low H_2O contents representing only OH^- groups is 88 ± 2 L/(mol·cm) (Dobson et al., 1989).

The band at 3710 cm^{-1}. Stolper et al. (1987) attributed this band to a combination of the ν_1 and ν_2 modes of $^{12}CO_2$. It is a low intensity band off the high energy shoulder of the OH^- band at 3570 cm^{-1}. The extinction coefficient, ϵ_{3710}, was determined in their study to be 13.9 L/(mol·cm) in albite glass.

The band at 4500 cm^{-1}. This band was assigned to the combination mode of Si-OH groups by Stolper (1982a). Newman et al. (1986) determined a value of 1.73 L/(mol·cm) for ϵ_{4500} in rhyolite glass. At low H_2O contents this band supplies the same information as does the band at 3570 cm^{-1}; the latter is used in this study because it is more intense.

The band at 4700 cm^{-1}. This band appears to be correlated to total CO_2 concentration. It is absent in the VNM50-15 starting material. At high CO_2 concentrations it appears as a roughly symmetric, narrow band beginning only a few wavenumbers from the high energy baseline of the 4500 cm^{-1} band. To our knowledge this band has not been identified in IR spectra of geological melts. We tentatively assign it to the first overtone of the $^{12}CO_2$ band at 2350 cm^{-1}.

Evaluation of uncertainty

Precision. The Beer-Lambert law describes the relationships among species concentration, band intensity, density, and sample thickness. The effect of the uncertainty in each of these variables contributes to the cumulative analytical precision. An uncertainty of ±3 μm was assigned to the measured thickness, and a standard deviation of ±10 g/L was determined for the density measurements. To find the standard deviation (1σ) of band-intensity measurements, 12 spectra were taken on the same spot of sample BF-153C. A band intensity of 1.5032 was determined for the CO_2 peak at 2350 cm^{-1} with an absolute standard deviation of ±0.0145 or a relative standard deviation of ±0.96%. Considering only the uncertainty in band intensity, these measurements translate into a CO_2 concentration of 2867 ± 28 ppmw. The precision of measured intensity is even better for the H_2O band at 3570 cm^{-1}, where for the 12 spectra an average band intensity of 0.21809 was determined with an absolute standard deviation of ±0.00152 or a relative standard deviation of 0.70%. This translates into an H_2O content of 1829 ± 13 ppmw.

If the uncertainty assigned to the thickness is treated as a standard deviation, this value along with the standard deviation in measured absorbance and density can be used to evaluate a total precision for measured concentration. For all the experimental samples, the result is a precision between 1.3 and 3.2% for CO_2 and the precision on measured H_2O is essentially the same. The factors affecting precision in order of decreasing importance

TABLE 2. Experimental results

Experiment no. (BF)	Duration (h)	P (bars)	f_{CO_2}* (bars)	d** (μm)	*Abs* (2350 cm^{-1})	CO_2 (ppmw)	CO_2 (ppmm)	*Abs* (3570 cm^{-1})	H_2O (ppmw)	H_2O (ppmm)	Comments†
					T = 950 °C						
134	69	1010	1315	146	0.43958	597	878	0.23667	1414	5079	T
152	328	1510	2290	170	0.81413	950	1397	0.21891	1123	4036	T
130	48	1993	3509	163	1.17733	1433	2095	0.48750	2608	9316	T
					T = 1050 °C						
111	15	504	566	375	0.35583	188	277	0.48583	1130	4065	T
123	46	1000	1291	275	0.68083	491	722	0.40500	1284	4615	T
124	42	1500	2241	248	0.99600	797	1173	0.31917	1122	4033	T
108	62	2025	3531	160	0.98533	1221	1794	0.24750	1349	4842	T
142	192	2040	3572	195	1.14994	1170	1723	0.15819	707	2544	T
128	43	2490	4977	121	0.94375	1547	2268	0.25600	1845	6607	T
139	70	3529	9545	157	1.59500	2015	2948	0.40167	2231	7973	I
153	96	4324	14699	103	1.35357	2607	3815	0.22167	1877	6711	I
153C‡	96	4324	14699	104	1.50320	2867	4195	0.21809	1829	6538	I
145	96	5496	25913	141	2.06500	2905	4242	0.38683	2393	8536	I
148	75	6612	42862	100	1.87083	3711	5398	0.35938	3134	11137	I
164	60	P_i = 2000	3461								
	108	P_i = 1000	1291	169	0.51051	599	883	0.11383	587	2115	T
					T = 1150 °C						
136	36	2029	3473	131	0.74333	1125	1657	0.10042	669	2407	I
149	96	3487	8941	136	1.22750	1790	2630	0.16667	1069	3838	I
131	16	4500	15192	174	2.05000	2337	3432	0.20333	1019	3656	I
147	77	5514	24416	148	2.13400	2860	4183	0.32604	1921	6864	I

Note: All concentrations calculated with a density of 2348 g/L.
* Calculated from the HSMRK equation of state (see text).
** d = thickness.
† T = TZM, I = IHPV.
‡ Not included in thermodynamic calculations.

are thickness, density, and absorbance; although the relative uncertainty in thickness changes dramatically with sample thickness. It is assumed that the uncertainties in measured absorbance of all other samples are identical to BF-153C. Although this is surely a simplification, it is probably a good approximation for most of the measured concentration range. Spectra of samples taken weeks apart fall within this range of precision.

Accuracy. The accuracy of these FTIR concentration measurements is difficult to evaluate. Contributing factors are the uncertainty in the extinction coefficient, sample heterogeneity, and the lack of suitable CO_2 standards of similar composition. The lack of rhyolite standards is a problem that cannot be addressed at this time, although if they were available, the current research would probably not be needed. As far as sample heterogeneity is concerned, almost all major heterogeneities were attributable to diffusion gradients. The procedure for determining equilibrium composition, including a more detailed description of sample heterogeneities, is outlined below (see Kinetics of CO_2 Solubility). Nevertheless, seven analyses were taken at seven places near the rim of sample BF-153 with sample thicknesses ranging from 97 to 106 μm. An average concentration of CO_2 at 2607 ± 92 ppmw (3.5%) and of H_2O at 1877 ± 68 ppmw (3.6%) was obtained. This is comparable to the standard deviations determined for multiple spot analyses of homogeneous samples.

The extinction coefficient of the band at 2350 cm^{-1} has been assigned a value of 945 ± 45 L/(mol·cm) (Fine and Stolper, 1985). If the arguments presented previously for use of this extinction coefficient with rhyolitic compositions are accepted, the accuracy of CO_2 concentrations due to the uncertainty in ϵ_{2350} is quantifiable. The ±45 L/(mol·cm) uncertainty in ϵ_{2350} is a standard error (Stolper et al., 1987). Conversion into standard deviation yields an absolute standard deviation of ±201 L/(mol·cm) or a relative standard deviation of ±21%. Similarly, the relative standard deviation of measured H_2O content resulting from the uncertainty in ϵ_{3570} is ±11% (Dobson et al., 1989).

EXPERIMENTAL RESULTS

The data

Results of CO_2-rhyolite experiments tabulated for each isotherm are presented in Table 2. The isotherm at 1050 °C was the most extensively studied and gives the most detailed information on both the Henry's Law region and the nonideal (in the Henrian sense) region. The isotherms at 950 °C and 1150 °C are most useful in delineating the effects of temperature on CO_2 solubility. In the diagrams that follow CO_2 concentrations are reported in ppm mole fraction (ppmm) or ppm weight fraction (ppmw). Fugacities of CO_2 were calculated with the hard-sphere modified Redlich-Kwong (HSMRK) equation of state of Kerrick and Jacobs (1981).

Henry's Law and nonideal regions

The portion of the 1050 °C isotherm adhering to Henry's Law is shown in Figure 2, where CO_2 concentration is plotted against f_{CO_2} for experiments up to 3.5 kbar. The figure shows a highly correlated linear trend between f_{CO_2} and dissolved CO_2 up to an f_{CO_2} of roughly 3550 bars (P

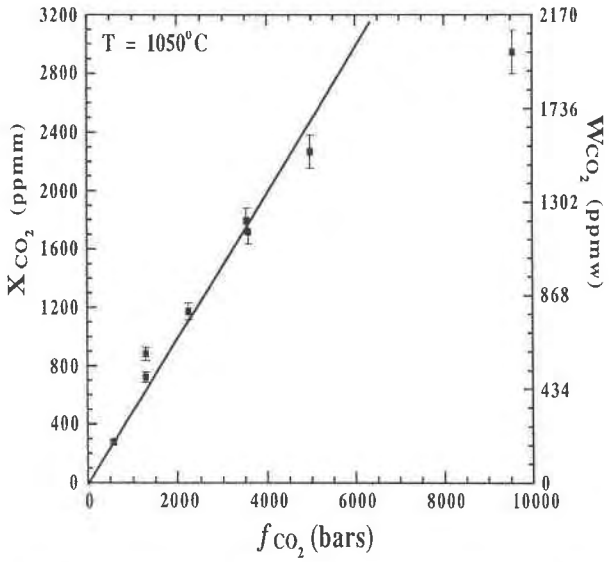

Fig. 2. Solubility of CO_2 in rhyolite melt as a function of f_{CO_2} for the low pressure region along the isotherm at 1050 °C. X_{CO_2} and W_{CO_2} are the mole and weight fractions of CO_2 in the melt in ppm, respectively. Error bars are 5% uncertainty encompassing precision of analyses and homogeneity. At low f_{CO_2} CO_2 solubility follows the linear form of Henry's Law. This is shown on the diagram by a straight line going through the region that behaves ideally.

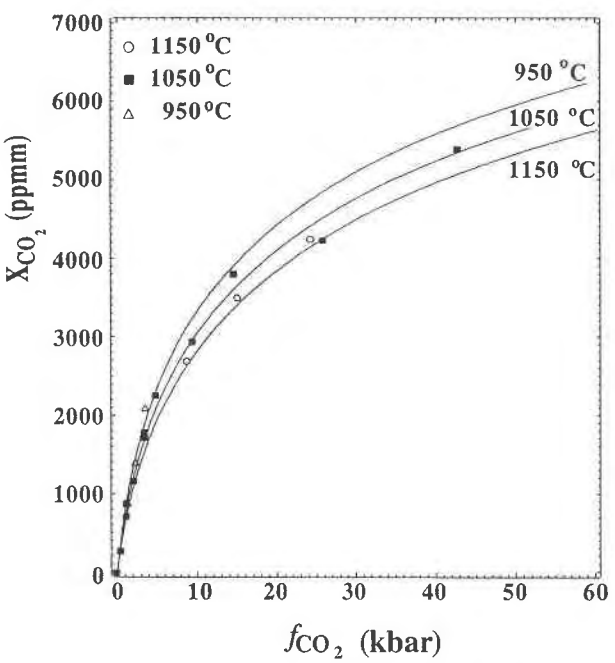

Fig. 3. Solubility of CO_2 in rhyolite melt as a function of f_{CO_2}, for the entire experimental region investigated. The isothermal solubility curves represent a least-squares regression through all the data. The experimental data show the strong deviation in CO_2 solubility from Henry's Law.

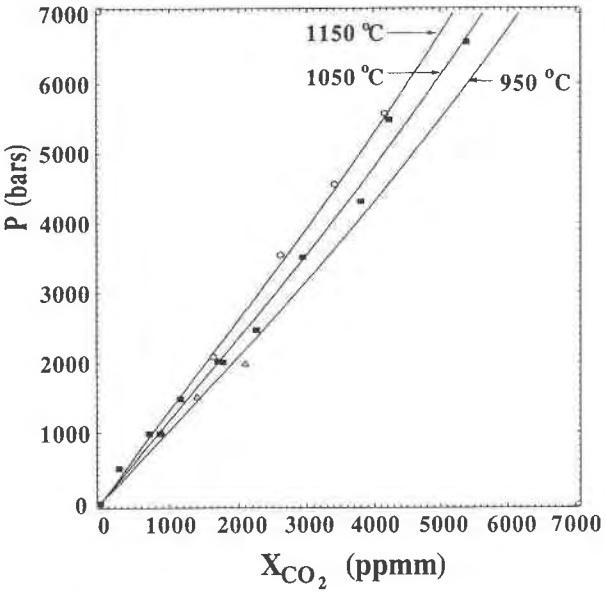

Fig. 4. CO_2 solubility as a function of total pressure. Isothermal solubility curves represent a least squares regression through all the data. The isotherms are roughly linear at low P and deviate from linearity at high P.

≈ 2050 bars). The first evidence of nonideality appears in the experiment with an f_{CO_2} of 4977 bars (P = 2490 bars), indicating that nonideality begins between 2050 and 2490 bars total pressure.

The nonideal region of CO_2 solubility is clearly distinguishable at pressures greater than ≈2500 bars (f_{CO_2} ≈ 5000 bars). This is shown in Figure 3, where f_{CO_2} is plotted against ppmm CO_2 for the entire experimental pressure range. For the temperatures of this study, the overall pressure dependence is roughly linear at low P and somewhat less than the linear prediction at high P (Fig. 4).

The experiments confirm a decrease in CO_2 solubility with increasing temperature. This is portrayed in Figures 3 and 4, where f_{CO_2} and P vs. ppmm CO_2 are contoured for temperature, respectively. This effect is similar to that observed for molecular CO_2 solubility in albite glass as determined by IR spectroscopy (Stolper et al., 1987). Sharma (1979) also reported a negative correlation between T and CO_2 solubility (in the form of CO_3^{2-}) in diopside and sodium melilite glasses using relative carbonate solubility as determined by Raman spectroscopy.

CO_2 solubility and H_2O concentration

The H_2O concentrations of all experimental glasses produced in this study are low, ranging from 500 to 3200 ppmw. There appears to be a positive correlation between CO_2 and H_2O concentration (Fig. 5); however, the highest H_2O contents on the isotherm at 1050 °C may be partly caused by the crystallization of feldspar in two experiments. BF-145 and BF-148, the two highest P experiments, contain ≈5 and 20% crystals concentrated on the

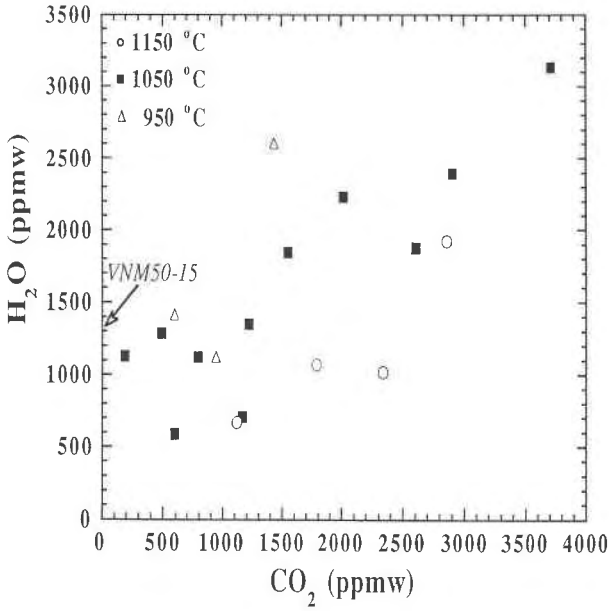

Fig. 5. CO_2 solubility vs. H_2O content of experimental samples. The starting composition is given by the arrow on the diagram.

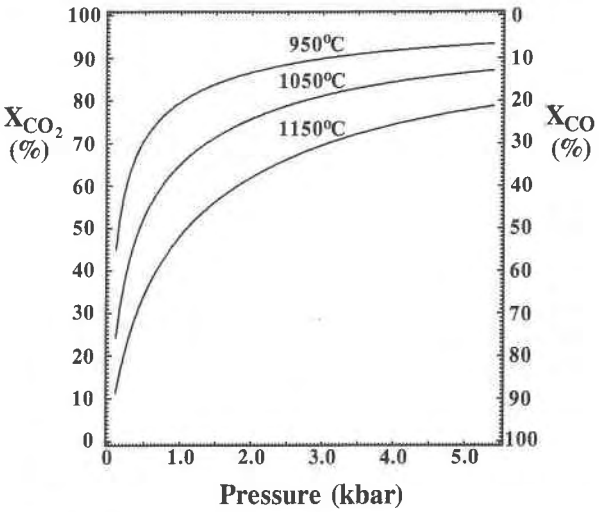

Fig. 6. Mole percent CO_2 and CO in the gas phase of the graphite-C-O system vs. pressure. Contoured isotherms indicate that for most of the experimental conditions, the lowest possible CO_2 content of the gas phase was 70%. Graphite was not detected in any of the experimental products, implying that the CO_2 content of the fluid was greater than that of the graphite-C-O system. Other information suggests that the amount of CO in the fluid phase was minimal (see text).

rim of the sample, respectively. A sample held at 7600 bars produced 70% crystals of feldspar and quartz, but a glass homogeneous in CO_2 was not found.

Although a positive correlation between CO_2 and H_2O is suggested by our data, little can be made of this correlation at this time. The experiments in this study were not designed to control for f_{H_2O}. The H_2O concentration of the experimental glasses is a function of the low initial H_2O concentration of the starting material (1366 ppmw), duration of the experiment (Table 2; compare BF-108 with BF-142 and BF-123 with BF-164), H_2 entering or leaving the sample during the experiment, and partitioning of H_2O between fluid and silicate liquid at extreme degrees of dilution. Calculations using the final H_2O and CO_2 content of the glasses suggest that less than 1 mol% H_2O was present in the fluid phase. One possibility for the positive correlation is the effect of increasing pressure on H_2O solubility. Higher pressures may favor the solubility of H_2O in the liquid over the vapor.

Fluid phase composition

As previously mentioned, the H_2O contents of the glasses indicate that the fluid phase contained only very small amounts of H_2O. It is possible, however, that conditions within the noble metal capsule were too reducing and produced substantial CO as well as CO_2. Several factors lead us to believe this was not a problem. First, some of the experimental glasses contained large bubbles of trapped fluid. FTIR spectra of these bubbles (accompanied by a computer-normalized subtracted spectra of a bubble-free portion of the glass) show a peak for gaseous CO_2. In contrast, spectra of bubbles in experimental rhyolitic glasses encapsulated with graphite and silver oxalate contain a peak centered about 2160 cm^{-1} that we attribute to gaseous CO. This suggests the relative absence of substantial gaseous CO in the vapor phase of the CO_2 solubility experiments. Second, if f_{O_2} conditions within the charge had been too low, graphite would have precipitated. Graphite has not been observed in any of our experimental products. Additionally, graphite-C-O fluid equilibria constrain the maximum amount of CO possibly present within the capsule. Figure 6 is a plot of the mol% CO_2 of the fluid in equilibrium with graphite for the three isotherms investigated in this study. Fluids in the graphite-C-O system become richer in CO_2 with increasing P and decreasing T. As illustrated, most of the experiments at 1050 °C have a minimum allowable molar CO_2 content of the gas in excess of 70%. Since graphite has not been found in any of the CO_2 solubility experiments, Figure 6 gives a minimum estimate of the concentration of CO_2 in the experimental fluids.

Kinetics of CO_2 solubility

With few exceptions, experimental glasses were removed from the capsules in the exact shape they were cut. This undoubtedly resulted from the very high viscosity of the rhyolitic melt. This observation implies that, other than mixing caused by vapor bubble infiltration, very little mixing of the melt occurred during the experiment and that the primary mechanism of equilibration was diffusion.

Many of the glasses from experiments of short duration contained diffusion profiles. Most experiment durations

TABLE 3. CO_2 diffusion in rhyolite at 1050 °C

Experiment (BF)	P (bar)	t (s)	Rim CO_2 (ppmm)	Core CO_2 (ppmm)	a (cm)	Dt/a^2	Log_{10} D
123	1000	165 600	722	273	0.168	0.163	−7.56
124	1500	151 200	1173	342	0.140	0.140	−7.74
128	2490	154 800	2268	759	0.164	0.145	−7.60
Average							−7.63

Note: Core and rim concentrations of CO_2 and relevant parameters for calculation of the diffusion coefficient of CO_2 in rhyolitic melt. Melt geometry is assumed to approximate a cylinder. The distance between measured rim and core concentrations = a, the duration of the experiment = t, and the dimensionless parameter Dt/a^2 is taken from Crank (1985).

were at least 48 h (Table 2). These long experiment times produced CO_2 diffusion profiles that extended over many hundreds of micrometers, often a millimeter, into the glass. In no case was a diffusion profile produced where the CO_2 concentration at the core of the sample reached a zero background—the amount of CO_2 in the VNM50-15 starting material. The core CO_2 concentration was almost always more than ⅓ the rim content. Apparently, the high melt viscosity helped keep the vapor phase exposed to the entire exterior of the melt.

Although experiments were done that produced homogeneous rim-to-rim CO_2 profiles, water often remained higher at the cores than at the rims. This is consistent with the exponential drop in H_2O diffusivity with total H_2O in rhyolite glass (Shaw, 1974). The magnitude of this diffusivity decay at very low H_2O contents (<0.5 wt%) is unknown, but our data suggest that the desorption of H_2O from rhyolite glass might be slower than the sorption of CO_2 into rhyolite glass at these T, P, X_{CO_2}(melt) and X_{H_2O}(melt).

For the experiments that contained diffusion profiles, the rim CO_2 concentrations were accepted as the equilibrium concentrations. The spot size analyzed in all FTIR spectra was never greater than 80 μm. Rim compositions were, therefore, averages of roughly the outer 80 μm of the sample. In these cases, spectra were also taken of the second 80 μm away from the rims and were found to have CO_2 contents only slightly (a few percent if at all) lower than the rim contents. One sample, BF-153, contained higher CO_2 concentrations in the core than at the rim. In this case, rim concentrations were still accepted as equilibrium concentrations. The cause of this reverse gradient is still not understood; however, both core (BF-153C) and rim (BF-153) compositions are presented in Table 2. Electron microprobe analyses of samples containing CO_2 diffusion profiles showed no major-element compositional heterogeneities.

With the realization that these experiments were not optimally designed to extract diffusion information, certain simplifying assumptions can be made to extract a qualitative value for the diffusivity of CO_2 into rhyolite melt at 1050 °C. We first assume charge geometry was cylindrical and that diffusion proceeded into the sample from all directions. Additionally it is assumed that the area of analyses was unaffected by diffusion into the liquid from the top and bottom of the cylinder. Having made these assumptions, knowledge of the experiment duration as well as the CO_2 concentration as a function of rim-to-core distance enables one to calculate the diffusion coefficients. The method reported in Crank (1985) for diffusion into a cylinder is used. Table 3 gives core and rim CO_2 concentrations of three experiments and other relevant information required for the calculation of $D_{1050\,°C}$; the diffusion coefficient of CO_2 in rhyolite at 1050 °C. The average value of $D_{1050\,°C}$ for the three experiments is 2.4 (±0.5) × 10^{-8} cm^2/s. These values compare favorably with that of Watson et al. (1982) for diffusion of CO_2 into a sodium aluminosilicate of composition 60% SiO_2, 30% Na_2O and 10% Al_2O_3 by weight. Their expression for D, uncorrected for pressure (negligible at P-T discussed here) yields 5.6 × 10^{-8} cm^2/s. In view of the approximations made to retrieve $D_{1050\,°C}$, the agreement between the two studies is excellent.

THERMODYNAMICS OF CO_2 SOLUBILITY

Henry's Law solubility

At extreme levels of dilution, the solubility of a volatile component within a liquid obeys Henry's Law. For the solubility of CO_2 in rhyolite liquid at constant T it is given as

$$f_{CO_2} = X_{CO_2} \cdot k_H \tag{3}$$

where f_{CO_2} is the fugacity of CO_2 in bars, X_{CO_2} is the mole fraction of CO_2 in the liquid, and k_H is the Henry's Law constant. This equation expresses a linear relationship between CO_2 solubility and fugacity. Figure 2 shows that CO_2 solubility in rhyolite obeys this law up to approximately 2300 bars total pressure; however, some concavity is apparent and results from the effect of pressure (see below). The Henry's Law constant determined with a least-squares regression of the data between 0 and 2000 bars for the isotherm at 1050 °C is k_H = 1.939 (±0.074) × 10^6 bar.

Above 2300 bars the linear form of Henry's Law (Eq. 3) is no longer applicable and must be modified to account for the effect of pressure. This is accomplished with the thermodynamic equality

$$\left(\frac{\partial \ln f_{CO_2}}{\partial P}\right)_{T,X} = \frac{\bar{v}}{RT} \tag{4}$$

to obtain the Krichevsky-Kasarnovsky equation (Prausnitz et al., 1986):

$$\ln\left(\frac{f_{CO_2}}{X_{CO_2}}\right) = \ln k_H + \frac{\bar{v}(P - P_r)}{RT} \quad (5)$$

where k_H is the Henry's Law constant at reference pressure P_r and $\bar{v}$ is the partial molar volume at infinite dilution of CO_2 in the liquid. Similarly, the following thermodynamic equality is used to modify Henry's Law to account for changes in temperature:

$$\left(\frac{\partial \ln f_{CO_2}}{\partial T}\right)_{P,X} = \frac{h^+ - \bar{h}}{RT^2} \quad (6)$$

where, h^+ and $\bar{h}$ are the molar enthalpy of CO_2 in the ideal gas state and the partial molar enthalpy of CO_2 in rhyolite, respectively. Henry's Law is then given by the expression:

$$\ln\left(\frac{f_{CO_2}}{X_{CO_2}}\right) = \ln k_H + \frac{\bar{v}(P - P_r)}{RT} + \frac{\bar{h} - h^+}{R}\left(\frac{1}{T} - \frac{1}{T_r}\right) \quad (7)$$

and can be rearranged to yield:

$$X_{CO_2} = \frac{f_{CO_2}}{k_H(P_r, T_r)} \exp\left[-\frac{\bar{v}(P - P_r)}{RT} - \frac{\Delta h}{R}\left(\frac{1}{T} - \frac{1}{T_r}\right)\right] \quad (8)$$

where Δh is the heat of solution of CO_2 given by $\bar{h} - h^+$ at P_r and $k_H(P_r, T_r)$ is the Henry's Law constant at P_r and T_r. At reference P and T, k_H is simply equal to $f_{CO_2}(P_r, T_r)/X_{CO_2}(P_r, T_r)$, making Expression 8 identical with that used by Stolper et al. (1987) for CO_2 solubility in albite melt.

Although the choice of P_r and T_r is somewhat arbitrary, there are factors that influence their selection. We select $P_r = 0$ for the following reasons: First, Prausnitz et al. (1986) pointed out that as $X_i \to 0$, P tends toward P^s, the saturation vapor pressure of the solvent. If we set $P_r = P^s$, Equation 8 is made more intuitively satisfying and directly expresses the functionality of the solubility process; the direct correlation of CO_2 solubility with P in excess of P^s. The value of P^s for rhyolite melt is unknown but is assumed to be close to 0 bars. Second, the selection of reference P only affects the Henry's Law constant and the enthalpy of solution. The partial molar volume of CO_2 in the melt is not affected by this selection. Although two of the constants change with P_r, the correlation coefficient, or the goodness of fit, does not change. T_r was selected as 1323 K since the isotherm at 1050 °C was investigated most thoroughly. For details and comments on the regression process see Appendix 1.

Thermodynamic results

Table 4 gives the values determined for k_H, $\bar{v}$, and Δh. The uncertainties given are the standard error of the estimates. The partial molar volume at infinite dilution is determined to be 33.04 ± 0.78 cm³/mol. This compares favorably with the work of Spera and Bergman (1980), who used the data of Mysen et al. (1976) and Mysen (1976) to determine the partial molar volume of CO_2 in albite, jadeite, and nepheline glasses to be 35–30 cm³/mol. These partial molar volumes are not directly comparable since, in addition to being of different composition, the glasses were produced at high T and P (1460 °C $< T <$ 1620 °C and 10 kbar $< P <$ 30 kbar), and contained large fractions of CO_2 dissolved as carbonate. A further complication is that the validity of the data presented by Mysen et al. (1976) has been called into question. Stolper et al. (1987) indicated problems with the experimental and analytical techniques of Mysen et al. (1976). The experiments of Mysen et al. (1976) were also shown to be inconsistent in the determination of CO_2 and CO_3^{2-} in albite with the Stolper et al. (1987) IR measurements. The partial molar volume presented here deviates somewhat from that of Stolper et al. (1987), who determined a value of 28.6 cm³/mol for CO_2 in albite melt. This value was determined with a regression through their data obtained in roughly the same P and T range as that of Mysen et al. (1976) and using the same analytical techniques as that used in this study.

Table 4. Solution model parameters

$$X_{CO_2} = \frac{f_{CO_2}}{k_H(P_r, T_r)} \exp\left[-\frac{\bar{v}(P - P_r)}{RT} - \frac{\Delta h}{R}\left(\frac{1}{T} - \frac{1}{T_r}\right)\right]$$

$P_r = 0$ bars; $T_r = 1050$ °C

X_{CO_2}*	Fluid**	$k_H(P_r, T_r)$ (10^6 bars)	$\bar{v}$ (cm³/mol)	Δh (kJ/mol)
Oxide	HSMRK	1.106 ± 0.038	33.04 ± 0.78	−20.32 ± 3.18
Eq-Ox	HSMRK	2.196 ± 0.075	32.88 ± 0.79	−20.64 ± 3.19
Oxide	MRK	1.080 ± 0.039	30.41 ± 0.83	−16.71 ± 3.38

Note: Uncertainties are reported as standard errors.

* Oxide = mole fraction oxide basis. Eq-Ox = mole-fraction equal O basis (see text).

** HSMRK = Hard sphere modified Redlich Kwong model of Kerrick and Jacobs (1981). MRK = Modified Redlich Kwong model of Holloway (1977).

One of the assumptions of the CO_2 solubility model is that $\bar{v}$ is not a function of P. Krichevsky and Kasarnovsky (1935) suggested that $\bar{v}$ may follow a simple relation with P such as

$$\bar{v} = \bar{v}^0 - \beta P \quad (9)$$

where $\bar{v}^0$ is the partial molar volume at 0 pressure and β is the coefficient of compressibility. Incorporation of this expression did little to improve the model and verified the initial assumption of the constancy of $\bar{v}$ with P.

Strictly speaking, the use of oxide mole fraction as the basis for calculating CO_2 concentration implies within the context of the solution model that all oxide components mix ideally in the melt. Although this implicit assumption is probably incorrect, the use of a more reasonable model does not significantly change the thermodynamic results. In accordance with the model of Stolper et al. (1987), the melt can be envisioned as an ideal mixture of O atoms, molecular CO_2, and carbonate molecules. Since carbonate complexes were not detected in this study,

CO_3^{2-} need not be included; however, H_2O in the form of OH^- ions should be included. This model assumes that melt O atoms, and molecular CO_2 molecules are each indistinguishable and that, in addition, OH^- ions are indistinguishable and mix ideally with both melt O atoms and CO_2 molecules. Stolper et al. (1987) pointed out some drawbacks of these assumptions, one of which is that in actuality there are probably many types of distinguishable O atoms in the melt. The advantage of this type of model is that the number of components is diminished, making the ideal mixing assumption more realistic.

X_{CO_2} was recalculated on this new basis by first putting all the melt-oxide components (excluding CO_2) on an equal O basis (multiplying the moles of each melt-oxide component by r, where r is the number of O atoms in the component, e.g., 2 for SiO_2, 3 for Al_2O_3). One half of the moles of H_2O (representing OH^-) was subtracted from the total moles of melt O atoms (Stolper, 1982b). The mole fraction of CO_2 was then recalculated and the model parameters redetermined. These are given in Table 4 along with the first set of parameters. A comparison of the two parameter sets shows that $\bar{v}$ and Δh are so slightly affected by this coordinate change that the standard errors of the two sets overlap. The main change is in the Henry's constant, which nearly doubles. From a mathematical perspective the differences in the parameter sets are straightforward. The basis change of components mainly affects the magnitude of X_{CO_2}, whereas the variation of X_{CO_2} with changes in P and T remains unaffected. It is the exponential term that controls these progressions, implying that the two data sets should give approximately the same $\bar{v}$ and Δh. The Henry's constant, however, is defined by $f_{CO_2}(P_r, T_r)/X_{CO_2}(P_r, T_r)$ and should be directly affected by changes in component selection. With the case at hand, recasting of the oxide components on an equal O basis results in a decrease in X_{CO_2}, which demands an increase in k_H. From a thermodynamic standpoint, the Henry's constant is directly related to the activity coefficient of the component, and activity coefficients must change with changes in basis components.

Equation 8 makes use of the f_{CO_2} as well as the solubility data reported in Table 2 to determine the thermodynamic constants k_H, $\bar{v}$, and Δh. Obviously then, the least-squares values determined for these constants depend upon the correct determination of f_{CO_2}, as well as the solubility data. Although the HSMRK equation of state (EOS) of Kerrick and Jacobs (1981) was used for this purpose, it is important to investigate the effects of a different f_{CO_2} on the thermodynamic constants. For this purpose we redetermined k_H, $\bar{v}$, and Δh using the f_{CO_2} calculated with the Modified Redlich Kwong (MRK) equation of state of Holloway (1977). The results (Table 3) show that the three constants are somewhat different, although not radically, from those calculated previously. Interestingly, $\bar{v}$ (30.4 cm³/mol) is now much closer to $\bar{v}$ in albite (28.6 cm³/mol) and results from the fact that the latter was determined with the MRK EOS (Stolper et al., 1987). The HSMRK model is considered to retrieve f_{CO_2} values superior to those obtained from the MRK model; Kerrick and Jacobs (1981) compared the two models.

Two other points concerning the use of this model are pertinent to this discussion. First, since different equations of state yield different f_{CO_2} and, hence, different CO_2 solubility constants, the use of Equation 8 is restricted to CO_2 solubility determinations with either one of these equations of state. Use of Equation 8 with f_{CO_2} determined with a third EOS may yield erroneous CO_2 solubilities. The solubility constants must be redetermined when the EOS of the fluid is changed because different fugacities are obtained from different equations of state. This situation exists because the lack of accurate PVT data at high P and T for CO_2 necessitates the use of an EOS with extrapolation capabilities. Second, since it is difficult to place an error on the f_{CO_2} calculations, the reported uncertainties on the model constants do not reflect errors in f_{CO_2}.

Discussion

The absence of carbonate

The lack of detectable CO_3^{2-} species in CO_2-saturated rhyolite glasses at pressures of up to 6.6 kbar is consistent with a trend of a decreasing ratio of CO_3^{2-} to CO_2(Mol.) with increasing silica activity (a_{SiO_2}) observed by Fine and Stolper (1985) for glasses along the $NaAlO_2$-SiO_2 join. Unpublished data from this laboratory on basalt, andesite, and rhyodacite melts equilibrated with a graphite-CO-CO_2 fluid show the same relationship between CO_3^{2-}/CO_2(Mol.) and activity of silica (a_{SiO_2}). The basaltic glasses contain dissolved carbonate with no detectable CO_2(Mol.), whereas the andesite and rhyodacite contain both CO_3^{2-} and molecular CO_2, with the latter increasing at the expense of the former in the more evolved liquids.

Because the basalt-rhyolite petrogenetic sequence involves numerous chemical trends, it is uncertain whether the apparent correlation between a_{SiO_2} and CO_3^{2-}/CO_2(Mol.) simply masks a more direct correlation of other cations such as Na_2O and CaO with CO_3^{2-}/CO_2(Mol.). The speciation data for the sodium-aluminosilicate system (Fine and Stolper, 1985) are also ambiguous in this respect, since the correlation of decreased CO_3^{2-}/CO_2(Mol.) with increased SiO_2 activity demonstrated in this system could equally well be due to decreases in Na_2O, Al_2O_3, or $NaAlO_2$ activity.

The ratio of CO_3^{2-} to CO_2(Mol.) may also be a function of the competition between CO_3^{2-} and Al^{+3} for charge balancing cations such as Na^{+1} (Brearley and Montana, 1989). If this paradigm is correct, it suggests that the ratio of CO_3^{2-} to CO_2(Mol.) is sensitive to the agpaitic index $K^* = (K_2O + Na_2O/Al_2O_3)$ of the melt. For $K^* < 1$ (peraluminous region) aluminum is in excess of alkalis, a condition that favors low ratios of CO_3^{2-} to CO_2(Mol.) because of stiff competition between CO_3^{2-} and Al^{+3} for charge-balancing cations. When K^* is greater than unity (peralkaline region), charge-balancing alkalis are in excess of aluminum, implying higher ratios of CO_3^{2-} to CO_2(Mol.)

resulting from free alkali cations not used by Al^{+3} for charge balancing. This idea is supported by the CO_2 solubility data in the system Na_2O-SiO_2 (Eitel and Weyl, 1932), which show high concentrations of CO_2 in solution at low pressures (8 wt% at 1250 atm and 1100 °C) in sodium-metasilicate glasses. The dominant form of CO_2 in these glasses is presumably carbonate and can reasonably be attributed to the absence of aluminum ($K^* = \infty$) which frees up Na for complex formation. This reasoning suggests that measurable quantities of carbonate would be present in peralkaline rhyolites of high K*.

Irrespective of the mechanism, these observations clearly indicate that the forward reactions in the equilibria

$$CO_3^{2-} \rightleftharpoons CO_2(\text{Mol.}) + O^{2-}_{(\text{melt})} \quad (10)$$

$$O^0_{(\text{melt})} + CO_3^{2-} \rightleftharpoons CO_2(\text{Mol.}) + 2O^-_{(\text{melt})} \quad (11)$$

are favored with progressive evolution in the basalt-rhyolite petrogenetic sequence. [O^0, O^-, and O^{2-} represent bridging, nonbridging, and free melt O atoms, respectively (Hess, 1980).]

The experiments presented here were all carried out at pressures below 6.6 kbar. We have no doubt that carbonate is present in these experimental glasses; albeit at levels below FTIR detection (roughly 50–100 ppmw for the techniques presented here). A progressive increase in pressure above 6.6 kbar should eventually bring carbonate levels above IR detectability limits. This contention is supported by the data of Fine and Stolper (1985), which indicate the presence of carbonate in CO_2-undersaturated experiments on $NaAlSi_4O_{10}$ glass at 25 kbar.

Rhyolite vs. albite

A comparison of CO_2 solubility in rhyolite and albite melts sheds some light on the solubility mechanism of CO_2(Mol.) in silicate melts. Figure 7 shows the solubility of CO_2(Mol.) in albite and rhyolite as a function of P contoured for T. The solution model of Stolper et al. (1987) was used to extrapolate their high P-T data down to the regions of this study. (CO_2 concentrations are compared on an equal O basis.) The CO_2(Mol.) solubility in the two compositions is remarkably similar; no significant departures exist up to 5 kbar. Departures in CO_2(Mol.) solubility between the two compositions become more acute with decreasing T and increasing P. Interestingly, total CO_2 solubility in albite is only slightly higher than CO_2(Mol.) solubility, with CO_3^{2-} composing only 2–3 mol% of total CO_2 at these pressures and temperatures.

The uniformity of CO_2(Mol.) solubility in rhyolite and albite melt at low pressures implies a similar, if not identical, solubility mechanism in the two compositions. This is probably the result of similarities in rhyolite and albite melt structures. Although rhyolite is more SiO_2-rich than albite, as far as CO_2(Mol.) solubility is concerned the basic melt structures are the same. This is supported by the data of Taylor and Brown (1979), who determined the radial distribution functions (RDF) for albite, anorthite, and orthoclase glasses and compared them with the RDF of pure SiO_2 glass. They showed that the RDF of albite and orthoclase melts are quite similar to SiO_2 melt, indicating that their basic melt structures are comparable. Rhyolite should also share this basic melt structure, since it falls within the SiO_2-$NaAlSi_3O_8$-$KAlSi_3O_8$ system.

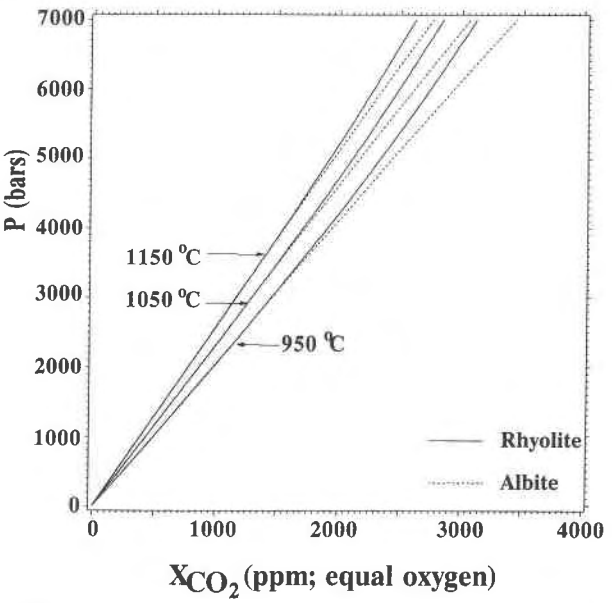

Fig. 7. CO_2 solubility as a function of pressure for rhyolite and albite. The isothermal curves for rhyolite were generated from the solution model in this study. The curves for albite were calculated from the CO_2 solubility model of Stolper et al. (1987).

The similarity in albite and rhyolite CO_2 solubility suggests that molecular CO_2 occupies the same sites in the two melts and that the solution mechanisms for these sites are comparable. Deviations from this behavior would be expected at high P and low T, conditions that tend to accentuate differences between melt structures and could lead to differences in solubility. This is exactly what is predicted for the two compositions (Fig. 7). These deviations could also be attributed to increased CO_2(Mol.) solubility at high P and low T. At high CO_2(Mol.) melt concentrations the siting of CO_2(Mol.) may differ in the two compositions, manifesting itself as differences in solubility.

Rhyolite vs. basalt

The data presented here and those of Stolper and Holloway (1988) can be used to compare the relative solubilities of CO_2 in rhyolite and basalt. The solubility of CO_2 in basalt at 1200 °C and 1000 and 1500 bars of total CO_2 gas pressure is 390 and 577 ppmw, respectively (Stolper and Holloway, 1988). This translates into 565 and 836 ppmm. With the solubility model presented here, the corresponding CO_2 solubility in rhyolite is 731 and 1100 ppmm, respectively. This contrast between CO_2 solubility in basalt and rhyolite is shown in Figure 8, where

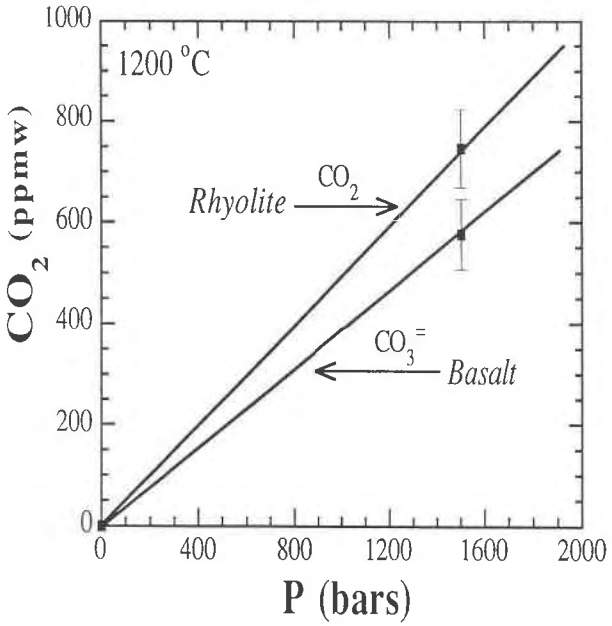

Fig. 8. Calculated CO_2 solubility in basalt (Stolper and Holloway, 1988) and rhyolite (this study) vs. CO_2 partial pressure. Error bars are standard errors. The solubility of CO_2 in rhyolite is greater than that in basalt. CO_2 dissolves in rhyolite solely in the molecular form, whereas in basalt it dissolves exclusively in the form of carbonate ions.

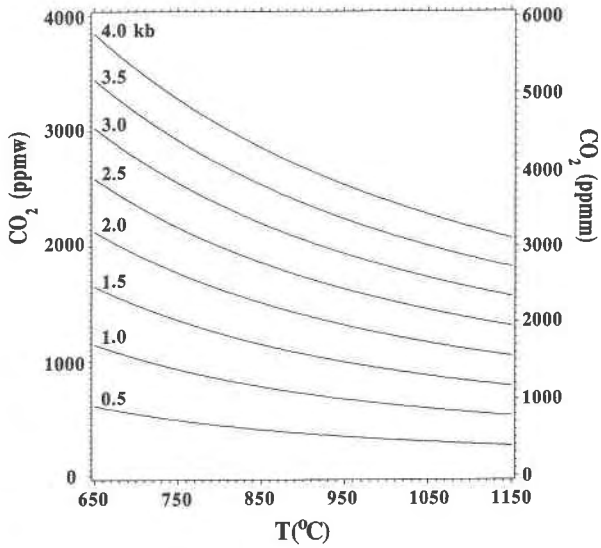

Fig. 9. CO_2 solubility as a function of temperature. Isobaric curves were calculated from the CO_2 solution model. The effect of temperature upon CO_2 solubility increases with increasing P and decreasing T.

CO_2 solubility is plotted against P_{CO_2} for 1200 °C. This demonstrates that on a molar basis CO_2 solubility in rhyolite is somewhat greater than in basalt, a situation that is true on a weight percent basis as well. Considering the uncertainty in the two data sets, the solubility of CO_2 in basalt and rhyolite is, at the least, comparable.

The comparison of CO_2 solubility data for basaltic and rhyolitic melts (Fig. 8) illustrates the two main differences in the behavior of CO_2 in these diverse liquids. First, the difference in CO_2 solubility between rhyolite and basalt is manifested in its mode of speciation. At low pressure, CO_2 dissolves in basalt as carbonate, whereas in rhyolite it dissolves in the molecular form. Second, the solubility of CO_2 in rhyolite is comparable to and somewhat greater than that in basalt at the same P and T. This demonstrates that the decrease in silica activity between rhyolite and basalt does not cause an increase in CO_2 solubility. This contrasts with the conclusions of many workers that CO_2 solubility decreases with increasing silica content (Eggler and Rosenhauer, 1978; Holloway et al., 1976; Mysen et al., 1976; Carmichael et al., 1974; Eggler, 1973). We reach this conclusion in spite of the conflict with some earlier works since (1) our analytical technique for rhyolite solubility is essentially identical to that of Stolper and Holloway (1988), who made the latest basalt solubility measurements, (2) the new data are based upon measured CO_2 concentrations and not implied from phase equilibria or other information, and (3) the accuracy of beta track autoradiography for CO_2 concentration measurements (Tingle and Aines, 1988) casts doubt on conclusions based upon data generated by this technique (e.g., Mysen et al., 1976). At this time, however, we can only make this comparison between basalt and rhyolite at pressures below 1500 bars.

Application to rhyolitic volcanism

The experimental data reported in this study is to our knowledge the first low-pressure solubility data for CO_2 in rhyolite melts. With the aid of the CO_2 solubility model, it is possible to extrapolate the results of this study to temperatures of rhyolitic volcanism in order to make estimates of magmatic CO_2 concentrations. The model can also be inverted to retrieve intensive parameters from known concentrations of CO_2 in rhyolite melt.

Our CO_2 solublity data have great potential for deciphering the evolution of rhyolitic magmas if the volatile contents of melt inclusions can be determined. In this vein, the relationship describing CO_2 solubility as a function of T and P is quite significant. The relationship between P_{CO_2} and CO_2 concentration is roughly linear at low P (Fig. 4). An a priori knowledge of magmatic P_{CO_2} and CO_2 concentration can yield magmatic T; however, a very accurate estimate of P would be required since the magnitude of the CO_2 solubility temperature effect is not large (Fig. 4). Unfortunately, magmatic P is rarely known with such accuracy. Conversely, knowledge of magmatic T and CO_2 concentration can yield P. Although the effect of T on CO_2 solubility is not drastic, it is still sufficiently great to require temperature estimates of high quality. Figure 9 shows the relationship between X_{CO_2}(Melt) and temperature as a function of P. At high T and low P $(\partial X_{CO_2}/\partial T)_P$ is close to 0. At moderate to high P and low T $(\partial X_{CO_2}/\partial T)_P$ is quite significant.

The fluid phase associated with rhyolitic magmatism usually contains a large, if not dominant, fraction of H_2O. At a given P and T H_2O will dissolve preferentially to CO_2 in rhyolite melt. The heterogeneous equilibria between fluid and magma with respect to CO_2 and H_2O are

$$CO_{2(fluid)} \rightleftharpoons CO_2(Mol.)_{(melt)} \quad (12)$$

$$H_2O_{(fluid)} \rightleftharpoons H_2O(Mol.)_{(melt)} \quad (13)$$

and the homogeneous equilibria within the melt are:

$$CO_2(Mol.) + O^{2-}_{(melt)} \rightleftharpoons CO_3^{2-} \quad (14)$$

$$H_2O(Mol.) + O^{2-}_{(melt)} \rightleftharpoons 2OH^-. \quad (15)$$

The two basic unknowns in the formulation of these equilibria are the extent of ideality of CO_2-H_2O mixing in the fluid phase, and the effect of dissolved H_2O and CO_2 on their mutual solubilities in the silicate melt. The lack of thermochemical data on CO_2-H_2O fluid mixtures at high P and T necessitates reliance on the predictive capacities of reasonably formulated equations of state. The HSMRK EOS of Kerrick and Jacobs (1981) predicts an extreme degree of nonideality between mixtures of these two gases. For small $X^{fluid}_{CO_2}$ the activity coefficient of CO_2 is predicted to be quite high. The same is true for the activity coefficient of H_2O for small $X^{fluid}_{H_2O}$. This further complicates the situation since CO_2 can reach high degrees of dilution ($X^{fluid}_{CO_2} \ll X^{fluid}_{H_2O}$) at magmatic conditions.

Currently, there is no consensus as to the effects of dissolved CO_2 and H_2O on their mutual solubilities in silicate melts. As a first approximation these effects can be assumed to be negligible. In actuality, since total dissolved CO_2 is quite low, both in an absolute sense as well as relative to H_2O, it is more likely that the effects of H_2O upon CO_2 will be more profound than the effects of CO_2 upon H_2O.

The solubility model describes the behavior of CO_2 solubility in rhyolite for all coexisting fluid-phase compositions that contain CO_2. When the fluid phase is pure CO_2, the solubility of CO_2 in rhyolite follows the behavior described by the model lines, shown as a function of P, T, and f_{CO_2} in the preceding diagrams. When the fluid phase is a mixture of CO_2 and some other species, CO_2 does not follow these curves. At constant T and P Equation 8 simplifies to

$$X_{CO_2} = \frac{f_{CO_2}}{k_H(P, T)} \quad (16)$$

where $k_H(P, T)$ is the Henry's constant at the specific P and T of interest and is given by

$$k_H(P, T) = k_h(P_r, T_r)\exp\left[\frac{\bar{v}(P - P_r)}{RT} + \frac{\Delta h}{R}\left(\frac{1}{T} - \frac{1}{T_r}\right)\right]. \quad (17)$$

X_{CO_2} is linear with changes in f_{CO_2} with the slope equal to $1/k_H(P, T)$. At constant T and P, the dilution of CO_2 fluid with another fluid species causes f_{CO_2} to be lowered and in a strict sense is given by

$$f^{Mix}_{CO_2} = a_{CO_2} \cdot f^{Pure}_{CO_2} \quad (18)$$

where a_{CO_2} is the activity of CO_2 in the fluid phase; thus, the accuracy of CO_2 solubility predictions under mixed fluid conditions is severely constrained by our ability to determine a_{CO_2}. The replacement of $a^{fluid}_{CO_2}$ with $X^{fluid}_{CO_2}$ as in the ideal mixing rule of Lewis and Randall can lead to questionable results.

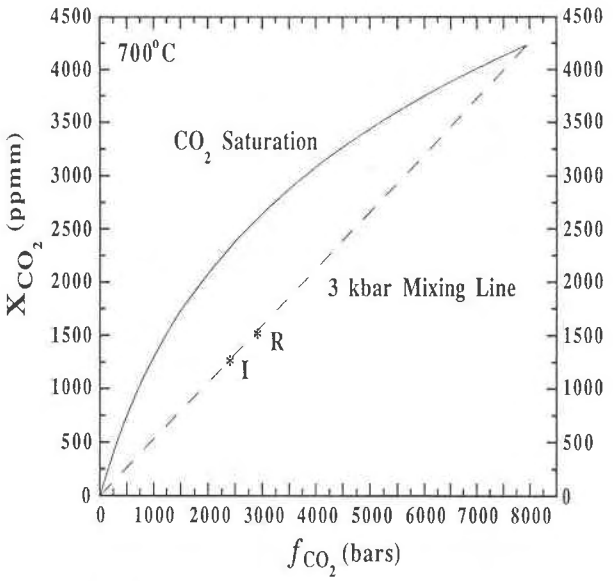

Fig. 10. The CO_2 saturation curve for 700 °C and pressures up to 3 kbar. At constant T and P, the presence of species other than CO_2 in the fluid decreases CO_2 solubility in direct proportion to $f_{CO_2}[X_{CO_2} = f_{CO_2}/k_h(P, T)]$. This type of mixing behavior is shown in the diagram for 3 kbar and 700 °C (3 kbar mixing line). If ideal mixing of a fluid containing 30% CO_2–70% H_2O (mol%) is assumed, the CO_2 solubility is found at point I. If one assumes HSMRK mixing of the fluid, the CO_2-solubility of the same fluid is found at point R.

The above discussion is illustrated in Figure 10, where both the CO_2 saturation curve and the 3 kbar CO_2 mixing line are plotted as a function of f_{CO_2} for T = 700 °C. At these conditions the dilution of fluid CO_2 with another fluid species such as H_2O displaces CO_2 contents down along the 3 kbar mixing line and not along the pure CO_2 saturation curve. Assuming ideal mixing, the predicted CO_2 solubility of a fluid containing 30% CO_2–70% H_2O (mol%) is 1316 ppmm (point I: $f^{Pure}_{CO_2}$ = 2384 bars). Assuming HSMRK behavior for the same fluid composition, the predicted CO_2 solubility would be 1594 ppmm (point R: $f^{Mix}_{CO_2}$ = 2887 bars) or 21% higher. The disparity becomes even greater with decreasing $X^{fluid}_{CO_2}$, increasing P, and decreasing T. Of course, the HSMRK EOS uses empirical mixing rules, and as such adds an element of uncertainty to these calculations. Additionally, if the solubility of H_2O affects the activity coefficient of CO_2 in the melt, the 3 kbar mixing line is distorted and would no

longer accurately represent CO_2 mixing conditions at 3 kbar. Clearly, the extent of ideality of the fluid mixing properties is a crucial element in the determination of CO_2 solubility under mixed volatile conditions and is a major consideration in the application of volatile solubility estimates to determine magmatic intensive parameters.

Conclusions

1. CO_2 solubility in rhyolite at 1050 °C follows a linear Henry's Law behavior to pressures of ≈2300 bars. Above this pressure CO_2 solubility rapidly becomes nonideal and deviates from the linear form of Henry's Law.

2. Results of experiments along the 950 °C, 1050 °C, and 1150 °C isotherms show a decrease in CO_2 solubility with increasing temperature.

3. H_2O concentrations below 0.32 wt% do not affect the speciation of CO_2 in rhyolite melt. A positive correlation between CO_2 solubility and H_2O content cannot be ruled out; however, the lack of f_{H_2O} control during the experiments, including other factors, makes this correlation suspect.

4. The diffusion of CO_2 into rhyolite appears to be the main mechanism for CO_2(fluid)-rhyolite equilibration. Diffusion of CO_2 into rhyolite is slow; the diffusion coefficient at 1050 °C is ≈2.4 (±0.5) × 10^{-8} cm^2/s.

5. CO_2 solubility data can be described by an extended Henry's Law model that considers the effects of pressure and temperature. These are related to the partial molar volume at infinite dilution and the heat of solution of molecular CO_2 in rhyolite melt. The values of $\bar{v}$ and Δh were determined to be 33.04 ± 0.78 cm^3 and −20.32 ± 3.18 kJ/mol, respectively.

6. CO_2 dissolves in rhyolite melt in the molecular form; CO_3^{2-} was not detected in any of the experimental products. This observation follows the general trend of an increasing ratio of CO_2(Mol.) to CO_3^{2-} in the sequence basalt, andesite, rhyodacite, rhyolite, with basalt showing no detectable molecular CO_2.

7. CO_2(Mol.) solubility in rhyolite and albite appear to be identical at low P and high T. This implies a similar solubility mechanism in the two compositions. Divergence of CO_2(Mol.) solubility in albite and rhyolite at high P and low T is consistent with accentuated differences in melt structure at these conditions and differences in the siting of CO_2(Mol.) at high CO_2 concentrations.

8. A comparison of CO_2 solubility in rhyolite and basalt at low pressures and 1200 °C shows that CO_2 is somewhat more soluble in rhyolite than in basalt. Solubility differences between the two magma types are primarily differences in speciation: CO_2 dissolves in basalt as carbonate complexes and in rhyolite as molecular CO_2.

9. CO_2 solubility data, along with H_2O solubility data and T estimates, can be used to make magmatic intensive parameter estimates from melt inclusion volatile determinations. For a given P and T, if rhyolite is in equilibrium with a CO_2 fluid mixture, CO_2 solubility is described by a cord extending from 0 solubility at f_{CO_2} = 0 bars to the pure CO_2 saturation surface on an X_{CO_2}-f_{CO_2} diagram. The solubility is found along this cord by determining the correct f_{CO_2} of the fluid mixture.

Acknowledgments

We would like to thank Dr. Joseph Devine for help with the microprobe analyses. We would like to also thank Dr. Ed Stolper and the Cal-Tech IR group for generously opening up their lab for a two-week introduction to quantitative IR analysis. This manuscript greatly benefited from the reviews of F.J. Spera, J.R. Holloway, and an anonymous reviewer. This research was supported by NASA grant NGT 50229 and NSF grant EAR-8708604.

References cited

Anderson, A.T., Newman, S., Williams, S.N., Druit, T.H., Skirius, C., and Stolper, E. (1989) H_2O, CO_2, Cl and gas in Plinian and ash-flow Bishop rhyolite. Geology, 17, 221–225.

Brearley, M., and Montana, A. (1989) The effect of CO_2 on the viscosity of silicate liquids at high pressure. Geochimica et Cosmochimica Acta, 53, 2609–2616.

Carmichael, I.S.E., Turner, F.J., and Verhoogen, J. (1974) Igneous petrology, 739 p., McGraw Hill, New York.

Crank, J. (1985) The mathematics of diffusion, 414 p., Clarendon Press, Oxford.

Dixon, T.E., Stolper, E., and Delaney, J.R. (1988) Infrared spectroscopic measurements of CO_2 and H_2O in Juan de Fuca Ridge basaltic glasses. Earth and Planetary Science Letters, 90, 87–104.

Dobson, P.F., Epstein, S., and Stolper, E.M. (1989) Hydrogen isotope fractionation between coexisting vapor and silicate glasses and melts at low pressure. Geochimica et Cosmochimica Acta, 53, 2723–2730.

Eggler, D.H. (1973) Role of CO_2 in melting processes in the mantle. Carnegie Institution of Washington Year Book, 72, 457–467.

Eggler, D.H., and Rosenhauer, M. (1978) Carbon dioxide in silicate melts: II. Solubilities of CO_2 and H_2O in $CaMgSi_2O_6$ (diopside) liquids and vapors at pressures to 40 kb. American Journal of Science, 278, 64–94.

Eitel, W., and Weyl, W. (1932) Residuals in the melting of commercial glasses. Journal of the American Ceramic Society, 15, 159–166.

Fine, G., and Stolper, E. (1985) The speciation of carbon dioxide in sodium aluminosilicate glasses. Contributions to Mineralogy and Petrology, 91, 105–121.

——— (1986) Dissolved carbon dioxide in basaltic glasses: Concentrations and speciation. Earth and Planetary Science Letters, 76, 263–278.

Fogel, R.A. (1989) The role of C-O-H-Si volatiles in planetary igneous and metamorphic processes: Experimental and theoretical studies. Ph.D. thesis, Brown University, Providence, Rhode Island, 201 p.

Gerlach, T.M. (1986) Exsolution of H_2O, CO_2 and S during eruptive episodes at Kilauea Volcano, Hawaii. Journal of Geophysical Research, 91, 12177–12185.

Gerlach, T.M., and Casadevall, T.J. (1986a) Evaluation of gas data from high-temperature fumaroles at Mount St. Helens, 1980–1982. Journal of Volcanology and Geothermal Research, 28, 107–140.

——— (1986b) Fumarole emissions at Mount St. Helens volcano, June 1980 to October 1981: Degassing of a magma-hydrothermal system. Journal of Volcanology and Geothermal Research, 28, 141–160.

Hess, P.C. (1980) Polymerization model for silicate melts. In R.B. Hargraves, Ed., Physics of magmatic processes, p. 3–48. Princeton University Press, Princeton, New Jersey.

Holloway, J.R. (1977) Fugacity and activity of molecular species in supercritical fluids. In D.G. Fraser, Ed., Thermodynamics in geology, p. 161–181. Reidel, Boston.

Holloway, J.R., Mysen, B.O., and Eggler, D.H. (1976) The solubility of CO_2 in liquids on the join CaO-MgO-SiO_2-CO_2. Carnegie Institution of Washington Year Book, 75, 626–631.

Johnson, M.C., and Rutherford, M.J. (1989) Experimentally determined conditions in the Fish Canyon Tuff, Colorado, magma chamber. Journal of Petrology, 30, 711–737.

Kerrick, D.M., and Jacobs, G.K. (1981) A modified Redlich-Kwong equa-

tion for H_2O, CO_2 and H_2O-CO_2 mixtures at elevated pressures and temperatures. American Journal of Science, 281, 735–767.

Krichevsky, I.R., and Kasarnovsky, J.S. (1935) Thermodynamical calculations of solubilities of nitrogen and hydrogen in water at high pressures. Journal of the American Chemical Society, 57, 2168–2171.

Mysen, B.O. (1976) The role of volatiles in silicate melts: Solubility of CO_2 and H_2O in feldspar, pyroxene and feldspathoid melts to 30 kbar. American Journal of Science, 276, 969–996.

Mysen, B.O., Eggler, D.H., Seitz, M.G., and Holloway, J.R. (1976) Carbon dioxide in silicate melts and crystals: Part I Solubility measurements. American Journal of Science, 276, 455–479.

Newman, S., Epstein, S., and Stolper, E. (1988) Water, carbon dioxide and hydrogen isotopes in glasses from the ca. 1340 A.D. eruption of the Mono Craters California: Constraints on degassing phenomena and initial volatile content. Journal of Volcanology and Geothermal Research, 35, 75–96.

Newman, S., Stolper, E.M., and Epstein, S. (1986) Measurement of water in rhyolitic glasses: Calibration of an infrared spectroscopic technique. American Mineralogist, 71, 1527–1541.

Prausnitz, J.M., Lichtenthaler, R.N., and Gomes de Azevedo, E. (1986) Molecular thermodynamics of fluid-phase equilibria, 600 p., Prentice-Hall, New Jersey.

Rai, S.C., Sharma, S.K., Muenow, D.W., Matson, D.W., and Byers, C.D. (1983) Temperature dependence of CO_2 solubility in high pressure quenched glasses of diopside composition. Geochimica et Cosmochimica Acta, 47, 953–958.

Roedder, E. (1965) Liquid CO_2 inclusions in olivine-bearing nodules and phenocrysts from basalts. American Mineralogist, 50, 1746–1782.

Rutherford, M.J., Sigurdsson, H., Carey, S., and Davis, A. (1985) The May 18, 1980, eruption of Mount St. Helens, 1. Melt composition and experimental phase equilibria. Journal of Geophysical Research, 90, 2929–2947.

Sharma, S.K. (1979) Structure and solubility of carbon dioxide in silicate glasses of diopside and sodium melilite composition at high pressures from Raman spectroscopy data. Carnegie Institution of Washington Year Book, 78, 532–537.

Sharma, S.K., Hoering, T.C., and Yoder, H.S. (1979) Quenched melts of akermanite compositions with and without CO_2—Characterization by Raman spectroscopy and gas chromatography. Carnegie Institution of Washington Year Book, 78, 537–542.

Shaw, H.R. (1974) Diffusion of H_2O in granitic liquids, Part I. Experimental data; Part II. Mass transfer in magma chambers. In A.W. Hoffman, B.J. Giletti, H.S. Yoder, and R.A. Yund, Eds., Geochemical transport and kinetics, Carnegie Institution of Washington Publication #634, 139–170.

Silver, L., and Stolper, E. (1989) Water in albitic glasses. Journal of Petrology, 30, 667–709.

Sommer, M.A. (1977) Volatiles H_2O, CO_2 and CO in silicate melt inclusions in quartz phenocrysts from the rhyolitic Bandelier air-fall and ash-flow tuff, New Mexico. Journal of Geology, 85, 423–432.

Spera, F.J., and Bergman, S.C. (1980) Carbon dioxide in igneous petrogenesis: I. Aspects of dissolution of CO_2 in silicate liquids. Contributions to Mineralogy and Petrology, 74, 55–60.

Stolper, E. (1982a) Water in silicate glasses: An infrared spectroscopic study. Contributions to Mineralogy and Petrology, 81, 1–17.

——— (1982b) The speciation of water in silica melts. Geochimica et Cosmochimica Acta, 46, 2609–2620.

Stolper, E., Fine, G., Johnson, T., and Newman, S. (1987) Solubility of carbon dioxide in albitic melt. American Mineralogist, 72, 1071–1085.

Stolper, E., and Holloway, J.R. (1988) Experimental determination of the solubility of carbon dioxide in molten basalt at low pressure. Earth and Planetary Science Letters, 87, 397–408.

Taylor, M., and Brown, G.E. (1979) Structure of mineral glasses, I. The feldspar glasses $NaAlSi_3O_8$, $KAlSi_3O_8$, $CaAl_2Si_2O_8$. Geochimica et Cosmochimica Acta, 43, 61–75.

Tingle, T.N., and Aines, R.D. (1988) Beta track autoradiography and infrared spectroscopy bearing on the solubility of CO_2 in albite melt at 2 GPa and 1450 °C. Contributions to Mineralogy and Petrology, 100, 222–225.

Tuttle, O.F., and Bowen, N.L. (1958) Origin of granite in light of experimental studies in the system $NaAlSi_3O_8$-$KAlSi_3O_8$-SiO_2-H_2O. Geological Society of America Memoir, 74, 153 p.

Watson, E.B., Sneeringer, M.A., and Ross, A. (1982) Diffusion of dissolved carbonate in magmas: Experimental results and applications. Earth and Planetary Science Letters, 61, 346–358.

Weast, R.C., and Astle, M.J. (1981) CRC handbook of chemistry and physics, CRC Press, Cleveland, Ohio.

Manuscript received June 19, 1990
Manuscript accepted September 13, 1990

Appendix 1. Least-squares regression

The experimental data were fitted to Equation 8 with the SAS procedure NLIN, a nonlinear least-squares routine (since Equation 8 is nonlinear) allowing constants k_H, $\bar{v}$, and Δh to vary so as to produce optimized values. P_r and T_r could have been chosen to be one of the experimental conditions and k_H determined as f_{CO_2}/X_{CO_2} from the data, a procedure that forces the least-squares regression through the reference conditions. Considering the error associated with any one point, or even a series of experimental points, leads to the conclusion that this type of fitting process does not produced optimum results.

Equation 7 is the linearized form of Equation 8 and could serve as the basis for a linear least-squares regression of $\ln(f_{CO_2}/X_{CO_2})$ vs. P for the entire data set in a manner similar to that used by Spera and Bergman (1980). The problem with this technique is the difficulty in fitting the data in the low pressure region, since the quantity $\ln(f_{CO_2}/X_{CO_2})$ is quite sensitive to small errors in X_{CO_2}. Deviations from linearity are accentuated in this region, and since the low pressure region is an end point of the $\ln(f_{CO_2}/X_{CO_2})$ vs. P line, it has a dominating effect upon the regression. This leads to a poor correlation of all the data and an underestimation of the partial molar volume term. In point of fact, the partial molar volume term should be controlled mostly by the high pressure region, where the effects of P on solubility are most important. Use of Equation 8 with the nonlinear least squares routine does not overly weight the data in the low pressure region and successfully reproduces the data with low residuals.